JGR Space Physics

RESEARCH ARTICLE
10.1029/2025JA034718

Key Points:

- We quantify the energy partition across a shock with upstream field nearly aligned with the shock normal
- A significant fraction of the incident energy is given to a small number of suprathermal and energetic protons
- Some of the energy fluxes are carried by field and plasma fluctuations that are prevalent at quasi-parallel shocks

Correspondence to:
S. J. Schwartz,
s.schwartz@imperial.ac.uk

Citation:
Schwartz, S. J., Trattner, K. J., Raptis, S., Ergun, R. E., Wilson, L. B., III, Gomez, R. G., et al. (2026). Energy partition at a collisionless supercritical quasi-parallel shock. *Journal of Geophysical Research: Space Physics*, *131*, e2025JA034718. https://doi.org/10.1029/2025JA034718

Received 30 SEP 2025
Accepted 16 FEB 2026

Energy Partition at a Collisionless Supercritical Quasi-Parallel Shock

Steven J. Schwartz[1,2], **Karlheinz J. Trattner**[2], **Savvas Raptis**[3], **Robert E. Ergun**[1], **Lynn B. Wilson III**[3], **Roman G. Gomez**[4], **Ian J. Cohen**[3], **Daniel J. Gershman**[5], **Katherine A. Goodrich**[6], **Harald Kucharek**[7], **and Tien Vo**[2]

[1]Imperial College London, London, UK, [2]Laboratory for Atmospheric and Space Physics, Boulder, CO, USA, [3]Space Exploration Sector, The Johns Hopkins Applied Physics Laboratory, Laurel, MD, USA, [4]Southwest Research Institute, San Antonio, TX, USA, [5]Goddard Space Flight Center, Greenbelt, MD, USA, [6]Department of Physics and Astronomy, West Virginia University, Morgantown, WV, USA, [7]University of New Hampshire, Durham, NH, USA

Abstract Shocks in collisionless astrophysical plasmas redistribute some of the incident flow energy into both thermal and non-thermal energy. Quantifying the partition of that energy amongst various particle species or their sub-populations, and electromagnetic energy, represents a fundamental goal of shock physics. It embodies the role of the equation of state for the system. Here we apply a framework to assess all the incident and downstream energy fluxes at a crossing of Earth's bow shock for which the upstream magnetic field was roughly aligned with the shock normal direction. Such quasi-parallel shocks are known to be non-steady and to produce significant populations of suprathermal particles. We quantify the evolution of all the important carriers of energy flux through the shock region. We sub-divide the proton population into thermal, suprathermal, and energetic components in order to investigate the shock's efficiency in energizing the nonthermal particles. While the largest energy fluxes are found in the incident proton ram energy and downstream proton thermal enthalpy fluxes, a significant suprathermal population pervades the regions both up- and downstream. We also evaluate the energy fluxes attributable to fluctuations in the fluid and field parameters.

Plain Language Summary Shock waves are driven in astrophysics by explosions and supersonic flows. Those shock waves convert much of the directed flow energy into less ordered forms. Typically, astrophysical plasmas are so rarefied that collisions between particles are ineffective in establishing a constant temperature amongst the electrons and ions. Consequently, some energy is concentrated in, for example, the acceleration of cosmic ray particles to high energies. The different particle and electromagnetic field components receive an unequal share of the energy. We investigate this problem of energy partition from a holistic perspective by analyzing comprehensive data from state of the art spacecraft that traverse shock waves in interplanetary space. We focus here on a shock which is intrinsically nonsteady and turbulent. Such shocks are known to produce energetic particles. The present work adds quantitative analysis to support that knowledge by placing those energetic particles in the context of the other energy carriers at the shock.

1. Introduction

In astrophysical plasmas, the scales over which shock waves dissipate energy are typically much smaller than the collisional mean free path. The processes required to decelerate the incident bulk flow and re-distribute its energy must be kinetic in nature. Those processes will have different impacts on the variety of plasma species and electromagnetic fields present, and occur over different scales. Sub-populations of the particles will heat more strongly than others, or may be accelerated to high energies (Kucharek et al., 2003). Fundamentally, the partitioning of the incident energy, or equivalently the equation of state, represents the key unanswered question in shock physics. Unraveling how the partition depends on shock parameters remains an important goal in, for example, the acceleration of cosmic rays.

The Earth's magnetosphere provides an obstacle to the supersonic solar wind flow, leading to the formation of a bow shock upstream of the Earth. This region of space has been accessible to in situ measurement by satellites carrying increasingly sophisticated instrumentation. Much of what we know about collisionless shocks has been gleaned from the data returned by these missions (Burgess & Scholer, 2015; Krasnoselskikh et al., 2013; Schwartz, 2006; Schwartz et al., 2013; Scudder, Mangeney, Lacombe, Harvey, Wu, et al., 1986; Stone & Tsurutani, 1985; Tsurutani & Stone, 1985).

Previous work concentrated on individual processes that might operate at collisionless shocks, including the reflection of ions (Paschmann et al., 1982; Sckopke et al., 1983; Woods, 1969), quasi-static fields (Gedalin, 2020; Schwartz et al., 2021; Scudder, Mangeney, Lacombe, Harvey, & Aggson, 1986), micro-instabilities and turbulence (Balikhin et al., 2023; Golan & Gedalin, 2025; Goodrich et al., 2018; Plank & Gingell, 2023; Scudder, Mangeney, Lacombe, Harvey, & Aggson, 1986; Wilson et al., 2014), particle acceleration (Amano et al., 2020; Kis et al., 2004; Kucharek et al., 2004), non-stationarity/shock reformation (Johlander et al., 2018, 2022; Madanian et al., 2021; Raptis et al., 2022), magnetic reconnection (Gingell et al., 2019, 2020; Wang et al., 2019) and others. Statistical studies have focused on isolated pieces of the partition problem, including the degree to which the downstream electron temperature depends on upstream conditions (Schwartz et al., 1988), statistical aspects of electron distribution functions at shocks in interplanetary space (Wilson et al., 2019a, 2019b, 2020), the fraction of ions reflected for a range of Mach numbers (Leroy et al., 1982), or the energy deposited in energetic particles (David et al., 2022; Zhou et al., 2020). Typically, Rankine-Hugoniot fluid shock jump conditions based on the bulk shock parameters (Mach number, plasma β, shock geometry, electron to ion temperature ratio) are often employed to supplement and support the observed quantities.

These targetted studies have taught us a great deal about the physics of collisionless shocks. However, the overarching energy partition problem has received less attention. In the past, the full set of accurate upstream and downstream parameters has not been available with sufficient quality. At the Earth's bow shock, for example, the solar wind proton ram energy provides the primary upstream energy flux. This cold, super-thermal solar wind proton beam requires a dedicated instrument to completely resolve its internal structure. The heating due to the reflection of protons at the shock or by other means dominates the downstream energy flux. The decimated pieces making up the proton distributions at and downstream of the shock requires full 4π resolution over a broad range of energies.

Other nonthermal energy fluxes, both upstream and downstream, can be found in features of the proton, electron, α-particle and other ion species' velocity-space distribution functions. These include sub-populations of particles accelerated to high energies. The details of the velocity space distribution functions of these particles in the solar wind present significant hurdles. Both the AC and DC electromagnetic fields contribute to the total energy fluxes on either side of a shock.

Crucially, examining the processes involved in the kinetic aspects of the energy partition problem through the shock transition layer also imposes temporal resolution requirements of order 1 s or less, comparable to electron scales, for many parameters.

In a previous paper (Schwartz et al., 2022) (hereinafter Sch22) we developed a comprehensive framework for tracking the energy fluxes using spacecraft data. We applied that framework to two crossings of the terrestrial bow shock under conditions in which the upstream magnetic field made a large angle with respect to the shock normal, known as quasi-perpendicular shocks. The successful application of the methodology was aided by the comprehensive suite of state-of-the-art plasma instrumentation onboard NASA's Magnetospheric Multiscale Mission (MMS) (Burch et al., 2016). That success was further aided by the fact that the quasi-perpendicular field geometry binds gyrating particles together, resulting in a relatively steady, laminar shock structure.

Here we attempt to apply the same methodology to a quasi-parallel bow shock. Under these field geometries, particles can more readily traverse the shock in both directions, some reaching upstream where they excite kinetic plasma instabilities. The resulting shocks are intrinsically non-steady, with turbulence, waves, and coherent structures called SLAMS (Schwartz, 1991; Schwartz et al., 1992). Backstreaming and energetic particles occupy both the extended foreshock upstream and the downstream plasma. Quasi-parallel shocks are the locally observable prototypes for cosmic ray acceleration in supernovae shocks and elsewhere (e.g., Kang & Jones, 2007; Park et al., 2015). The non-steady fluctuations and waves offer new avenues for energy partition that we explore below.

The next sections summarize the data and our primary analysis methods. We then present our results and provide some discussion before drawing our final Summary and Conclusions.

2. Data

Our primary results are drawn from the Magnetospheric Multiscale mission (MMS) (Burch et al., 2016). We also used data from the Wind (Harten & Clark, 1995; Wilson et al., 2021) spacecraft to establish the prevailing interplanetary conditions. THEMIS C (Angelopoulos, 2008) is upstream and much closer than Wind to MMS; we employ that spacecraft to determine the unperturbed interplanetary magnetic field. Wind and THEMIS C data are lagged from their locations to that of MMS by comparing magnetic field clock angles. At the dayside bow shock, this angle is approximately preserved on passage through the shock to MMS when that spacecraft is in the shocked magnetosheath.

The main analysis relies on MMS data from the Fast Plasma Investigation (FPI) (Pollock et al., 2016), Fluxgate Magnetometer (FGM) (Russell et al., 2016), electric field instrumentation (Ergun et al., 2016; Lindqvist et al., 2016; Torbert et al., 2016), Hot Particle Composition Analyzer (HPCA) (Young et al., 2016) and Energetic Ion Spectrometer (EIS) (Mauk et al., 2016). We employed moment sums drawn from the FPI and other instrument public L2 data files. All of our detailed analysis utilized MMS data returned in burst mode. Burst data has better time resolution, notably FPI electron data at 30 ms and FPI ion data at 150 ms cadences, than survey data products. Additionally, FPI burst data is free from artifacts introduced into the compression algorithms for fast survey data. We subset the FPI ion (essentially proton) measurements into "thermal" and "suprathermal" components. We calculate the thermal protons by integrating the proton distribution from 11 eV (removing the bottom three energy channels to minimize the impact of counting statistics at low energies) to 4 keV. Suprathermal protons are integrated from the next energy channel at 5.3–28.3 keV. This division ensures that the suprathermal population is relatively free of contamination by solar wind alpha particles, which are unresolved in FPI's E/q instrumentation. Energetic Ion Spectrometer data completes the proton energy coverage from 32 to 800 keV. In Sch22 we provided some discussion and quantitative assessment of the errors in some of the measurements and how those propagate into the results.

For the interval we examine in detail below, MMS HPCA measurements of the solar wind alpha particle population suggest alpha densities of 0.5–0.6 cm^{-3}, that is, significantly higher than those reported by Wind, by up to a factor of 5–6. The HPCA RF proton attenuation system (Burch et al., 2016; Gomez et al., 2019; Young et al., 2016) reduces proton contamination of the alpha channel by lowering the comparatively higher proton flux, while allowing more massive ions to pass through the electrostatic analyzer. The proton attenuation depends on the HPCA unit used to make the measurement. During this measurement period, the proton flux was reduced by half for the HPCAs on MMS 1 and 2, and reduced by 90% for those on MMS 3 and 4. As a result, measurements made with MMS 3 suffer from less proton contamination, so we use it for all our MMS measurements. Backstreaming suprathermal alphas upstream of the shock may represent a real local enhancement of the alpha density by comparison to the far-upstream conditions.

HPCA's energy and angular resolutions are inadequate for fully resolving the solar wind alpha distribution, which is typically highly localized in energy and solid angle. Hot Particle Composition Analyzer has a large geometric factor and is designed to measure broadly distributed "hot" ion distributions. The solar wind, as a relatively "cold" ion distribution, is undersampled by HPCA. HPCA's proton attenuation and geometric factor work in opposite directions: proton contamination, if present, leads to higher densities, while unresolved velocity-space misses a significant fraction of the population. The magnetosheath alpha particle distributions, with their larger occupation of phase space, are an optimum target for HPCA's geometric factor. The broadened span of the proton distribution also makes proton attenuation more effective over a larger range. Thus, they are both well-resolved and well-separated from the protons by HPCA.

3. Mathematical Framework

3.1. Primary Analysis

The full mathematical framework for our analysis was laid out in Sch22. Here we briefly summarize the key ingredients.

We will work in the Normal Incidence Frame (NIF) in which the upstream velocity is antiparallel to the shock normal vector. The full transformation to the NIF from the spacecraft frame of reference is accomplished by subtracting the velocity

$$\mathbf{V}^{SC2NIF} = V_n^{sh}\mathbf{n} + \mathbf{V}^{up,SC} - \mathbf{n}\left(\mathbf{V}^{up,SC}\cdot\mathbf{n}\right) \tag{1}$$

where V_n^{sh} is the signed velocity of the shock along the shock normal as measured in the spacecraft frame, $\mathbf{n}$ is the upstream-pointing shock normal, and $\mathbf{V}^{up,SC}$ is the bulk solar wind velocity measured in the spacecraft frame (see Figure 1c and Equation 5 in Schwartz et al. (2021)).

The total energy conservation equation is

$$\frac{\partial \mathcal{E}}{\partial t} + \nabla\cdot\mathbf{F} = 0 \tag{2}$$

where $\mathcal{E}$ is the energy density and $\mathbf{F}$ the total energy flux. In a multispecies plasma the energy flux can be written:

$$\mathbf{F} = \mathbf{E}\times\mathbf{B}/\mu_o + \sum_{species\ j}\mathbf{Q}_j \tag{3}$$

where

$$\mathbf{Q}_j \equiv \int \mathbf{v}\,\frac{1}{2}m_j v^2 f_j(\mathbf{v})\,d^3v \tag{4}$$

$$= \mathbf{q}_j + \tag{5}$$

$$+\underline{\underline{\mathbf{p}}}_j\cdot\mathbf{u}'_j + \frac{3}{2}p_j\mathbf{u}'_j + \tag{6}$$

$$+\mathbf{u}'_j\frac{1}{2}\rho_j u_j'^2 \tag{7}$$

with $\mathbf{q}_j$ in (5) being the intrinsic heatflux as measured in the species' own rest frame, $\mathbf{u}'_j$ the bulk velocity of that species in the frame of interest (e.g., the NIF), (6) providing an expression for the enthalpy flux in terms of the species' intrinsic pressure tensor $\underline{\underline{\mathbf{p}}}_j$, and (7) being the ram energy flux associated with the species bulk flow. At a steady planar shock (2) reduces to

$$\mathbf{F}\cdot\mathbf{n} \equiv F_n = \text{constant} \tag{8}$$

It is often convenient to separate the protons, for example, into thermal and suprathermal components as described above. We consider and analyze each of these populations as a separate "species." Note that since protons are not tied to a unique sub-population, the proton continuity equation expressing conservation of protons would apply only to their aggregate, not to each sub-population.

3.2. Consideration of Steady, Planar Assumptions

As the quasi-parallel shock is highly variable, with multiple apparent crossings back and forth, it is often difficult to determine many shock parameters with total confidence. In applying the above formulation based on a steady, planar shock we employ the variability in, for example, total energy flux as an indicator of the impact of shock variability. At the same time, we employ the overall trends and similarities over the many crossings to determine at least semi-quantitatively the shock partition from a larger system perspective. That bigger picture is perhaps more interesting for extrapolating to other astrophysical environs.

In particular, the shock speed V_n^{sh} cannot be precisely determined. The back and forth motion implies that the shock never moves far from the spacecraft nor particularly fast, and we shall ignore the contribution terms involving V_n^{sh} make to energy fluxes. In any event, those contributions would oscillate in sign with every back and forth motion, are captured by the full time series of the energy fluxes shown below, and would average out over the longer term under steady interplanetary conditions.

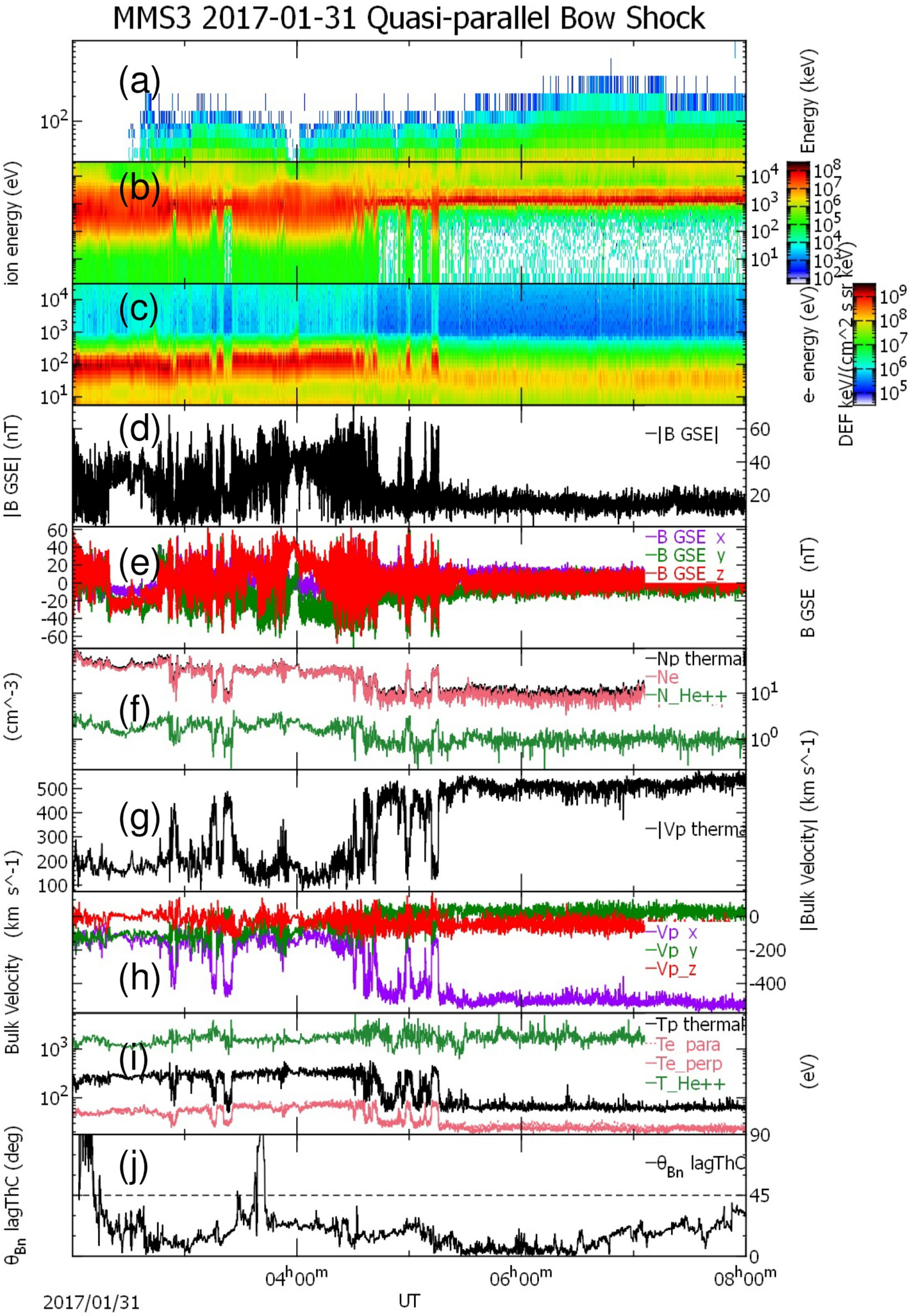
MMS3 2017-01-31 Quasi-parallel Bow Shock
(a)
(b)
(c)
(d)
(e)
(f)
(g)
(h)
(i)
(j)
10^2
Energy (keV)
ion energy (eV)
10^4
10^3
10^2
10^1
10^8
10^7
10^6
10^5
10^4
10^3
10^2
e- energy (eV)
DEF keV/(cm^2 s sr keV)
10^9
10^8
10^7
10^6
10^5
|B GSE| (nT)
—|B GSE|
60
40
20
—B GSE_x
—B GSE_y
—B GSE_z
B GSE (nT)
60
40
20
0
-20
-40
-60
(cm^-3)
—Np thermal
—Ne
—N_He++
10^1
10^0
—|Vp therma
|Bulk Velocity| (km s^-1)
500
400
300
200
100
Bulk Velocity (km s^-1)
—Vp_x
—Vp_y
—Vp_z
0
-200
-400
—Tp thermal
—Te_para
—Te_perp
—T_He++
(eV)
10^3
10^2
θ_{Bn} lagThC (deg)
—θ_{Bn} lagThC
90
45
0
2017/01/31
04^h00^m
06^h00^m
08^h00^m
UT

Figure 1.

Additionally, we assume the shock normal vector **n** is constant, as determined from a model bow shock (Slavin & Holzer, 1981) scaled to the location of MMS. At quasi-parallel shocks, time variability and spatial inhomogeneities make this assumption difficult to justify in anything other than a statistical sense, although Toy Edens et al. (2025) show that the model **n**'s outperform local determinations for many purposes.

Magnetic structures (SLAMS) form a key concept in macroscopic quasi-parallel shock geometry (Schwartz & Burgess, 1991). Longmore (2005) employed single-spacecraft normal determinations at different locations around SLAMS using multispacecraft analysis (Longmore, 2005) of the geometry of SLAMS observed by the four Cluster spacecraft. That study revealed that the typical variability in the normal directions along the SLAMS surface is of order $\lesssim 20°$. This variability translates to a variability in the normal component of a measured vector flux of 6%. Interestingly, SLAMS convect systematically toward the downstream state and represent a sort of reformation process that does not correspond to the back and forth motion discussed above.

The variability coupled with the close spacing of the MMS spacecraft (5 km here) doesn't allow us to employ any of several other methods to determine **n** or V_n^{sh} (see Schwartz (1998)). To date, limited attempts have been made to relax this assumption of constant **n** in shock analysis (Zank et al., 2021).

4. Overview of Quasi-Parallel Bow Shock of 31-01-2017

The first segment of the shock episode we shall analyze was previously studied by Trattner et al. (2023) in connection with the detailed production of diffuse ions. Table 1 summarizes the solar wind conditions prevalent on 31-01-2017 around 03:20. Most of these values are unremarkable in comparison with typical solar wind observations. Apart from these overall shock parameters as summarized in Table 1, our detailed analysis employs MMS data exclusively for internal consistency.

Figure 1 provides an overview of the MMS3 observations for a period of 6 hrs. The interplanetary magnetic field remains in a quasi-parallel orientation with respect to the model shock normal at the position of MMS for much of this period (panel (j)). Additionally (not shown), the interplanetary plasma conditions remain relatively steady, with a small gradual increase in overall solar wind speed by 50 km/s over a 4 hr interval. Consequently, we attribute most of the variability in the MMS observations to the inherent quasi-parallel shock processes.

A significant population of suprathermal and energetic protons can be seen in panels (a) and (b) throughout this interval extending from the top portion (>4 keV) FPI energy range into that of EIS. Later sections will sub-divide the proton population to study the distribution of energy into different energy bands. As is common at quasi-parallel shocks, the spacecraft makes numerous passes from the narrow solar wind beams to broadened magnetosheath-like distributions. For convenience, we shall use "upstream" or "solar wind" or "unshocked" to refer to the narrow beam regions and "downstream" or "shocked" to refer to the intervals of broadened, heated distributions. As is often the case for quasi-parallel shocks, this nomenclature is more qualitative than a clear identification of shock crossing from, for example, unshocked to shocked states.

5. Energy Fluxes

We now apply the methodology developed in Sch22 and summarized in Section 3. We use the MMS burst data that is available for the interval shown in Figure 1 to evaluate the normal components of the Poynting flux, heat fluxes, enthalpy fluxes, and ram energy fluxes in the NIF frame, neglecting $\mathbf{V}_n^{sh}$ as discussed above. The full resolution result is shown in Figure A1 in the Appendix. Here, Figure 2 shows those full resolution fluxes smoothed with a 20s sliding window.

Figure 1. Overview of MMS3 observations taken in survey mode on 31-01-2017. Proton differential energy flux from MMS Energetic Ion Spectrometer (a) and Fast Plasma Investigation (b) instruments together with the electron differential energy flux (c). Magnetic field magnitude (d) and components (e, f) Densities of the proton thermal population (black), electrons (pink) and alpha particles (green). The magnitude (g) and components (h) of the bulk velocity of thermal protons (11 eV–4 keV). Temperatures (i) of those thermal protons (black), parallel and perpendicular electron temperatures (pink) and alpha particles (green). The reported elevated alpha temperature suggests that the upstream alphas are contaminated by backstreaming particles, or that the solar wind alpha beam is not properly resolved, or both. Panel (j) shows the expected shock geometry θ_{Bn} based on the lagged THEMIS C magnetic field data, confirming that the interplanetary conditions remain quasi-parallel, well below 45°, for several hours.

Table 1
Solar Wind Conditions on 31-01-2017

Parameter	Value	Comments
MMS Position	(9.69, −6.63, 1.06)	R_e GSE @ 03:20 UT
Wind Position	(221.6, 100.0, −2.4)	R_e GSE @ 01:30 UT
THEMIS C Position	(48.0, 34.5, −1.3)	R_e GSE @ 02:40 UT
Wind lag to MMS	1 hr 26 min	Using clock angle
THEMIS C lag to MMS	22 min	Using clock angle
Wind interval (post-lag)	03:12–03:30	Most parameters
THEMIS C interval (post-lag)	03:03–03:48	
Magnetic field $\mathbf{B}$	(10.2, −4.7, 2.2)	nT GSE from THEMIS C
Proton density n_p	6.11	cm^{-3}
Alpha density n_α	0.105	cm^{-3}
Electron density n_e	6.32	cm^{-3} from charge neutrality
Proton velocity $\mathbf{V}_p$	(−504.6, −31.2, −28)	km/s GSE
Proton temperature T_p	18.4	eV
Alpha particle temperature T_α	76.1	eV
Electron temperature T_e	19	eV
Model shock normal vector $\mathbf{n}$	(0.932, −0.358, 0.057)	GSE using Slavin and Holzer (1981)
Angle between B and $\mathbf{n}$	9^o	
Proton plasma beta β_p	0.344	
Alpha plasma beta β_α	0.024	
Electron plasma beta β_e	0.368	
Total plasma beta β	0.737	
Alfvén Mach number V_A	4.7	
Fast Magnetosonic Mach number M_f	4.6	

Despite the significant fluctuations which survive the smoothing, Figure 2 reveals several mainly unsurprising features. The thermal protons carry the lion's share of the energy flux (panel (h)) and that is an interchange (see also panel (i)) between the ram energy (panel (d)) and enthalpy flux (panel (e)). The alphas make substantial contributions to the ram and enthalpy fluxes, followed by the suprathermal protons. Curiously, both thermal and suprathermal protons have intrinsic heatfluxes persistently directed upstream (i.e., below the dashed line in panel (f)). These heatfluxes are perhaps best interpreted as distortions or multi-component influences of the nonequilibrium particle phase space distributions. In what follows, we include these fluxes in our discussion of the roles played by the different populations.

We focus on the interval from 03:10 to 03:35 previously studied by Trattner et al. (2023) in Figure 3. At this scale, the exchange between ram and enthalpy fluxes is clear (see panel (i) around 03:20) together with the dominant role in the exchange played by the thermal protons (panels (d) and (e)). The crossing at 03:21, just after the shaded interval, provides a clean but representative characterization of the different flux carriers. By inspection from the panels at this time (see also Figure 6), we observe:

1. Roughly 70% of the total $\sim 1000 \mu W/m^2$ energy flux is incident in the form of thermal proton ram energy.
2. The remainder is nearly equally split between alpha-particle ram energy and incident thermal proton enthalpy flux.
3. Two thirds of that upstream thermal proton enthalpy flux is offset by the thermal proton heat flux carrying energy back upstream.
4. Downstream, 20% of the total energy flux remains in thermal proton ram energy with another 5% in alpha ram energy.

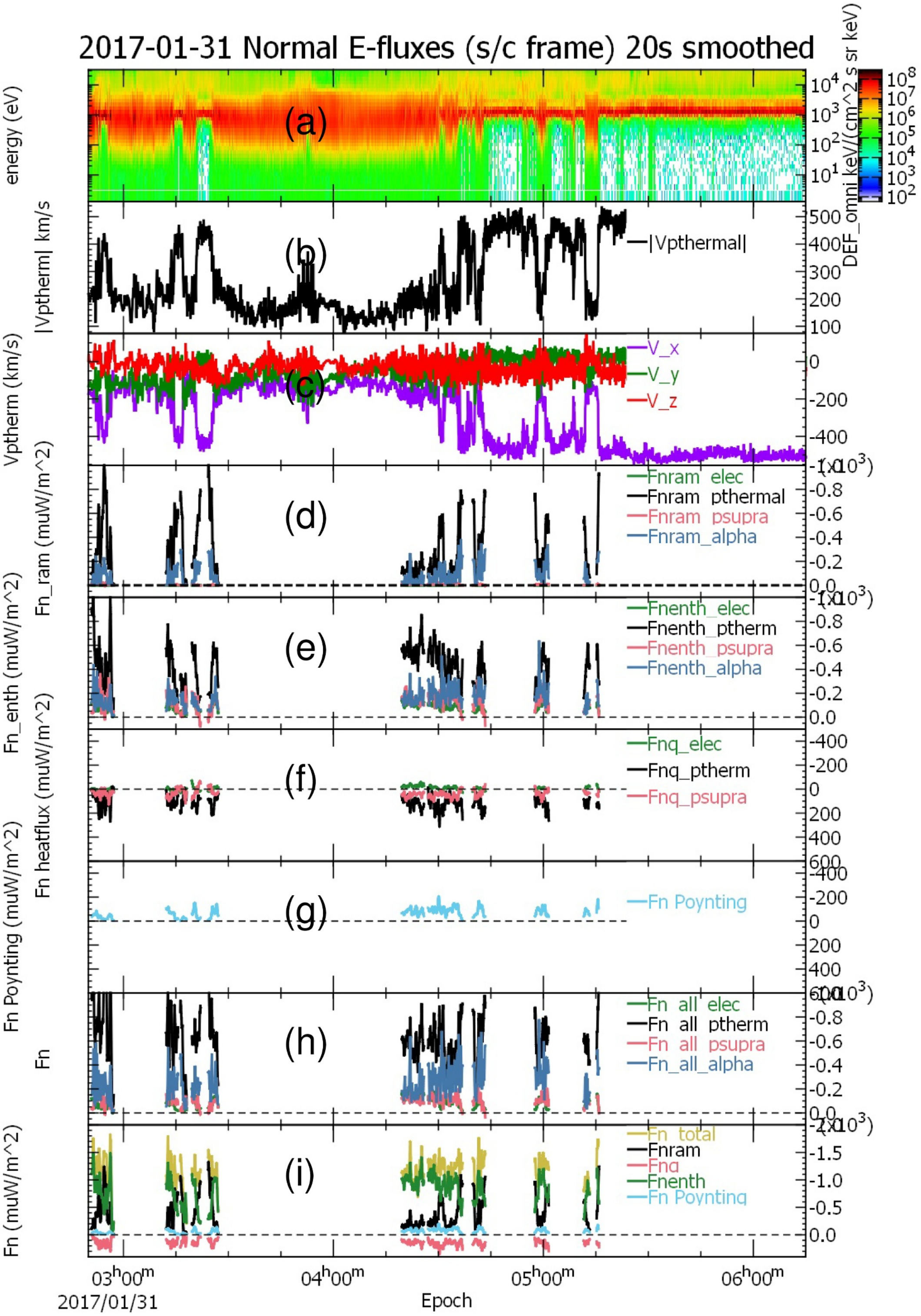

Figure 2. Normal components of the various contributions to the energy fluxes in the Normal Incidence Frame shock rest frame (assuming $V_n^{sh} = 0$), smoothed with a 20s sliding window. Panels (a–c) show the fast survey ion differential energy flux and bulk velocity of the thermal protons. The remaining panels use intervals for which burst mode data was available. Panels (d–f) show the ram, enthalpy and intrinsic heat energy fluxes for the electrons (green), thermal protons (black), suprathermal protons (red) and alpha particles (blue). Panel (g) shows the normal Poynting flux. In panel (h) we collect the particle fluxes by species, while panel (i) collects the fluxes by type together with (gold) the total energy flux. With the exception of panel (i), all flux panels have the same total range of values. Additionally, since the main incident fluxes are oppositely directed to the outward-pointing shock normal, we have inverted the direction of the flux panels so that fluxes above the dashed zero lines are directed from the upstream, unshocked state, to the downstream.

5. Nearly half the downstream energy flux is carried by thermal proton enthalpy flux, with a further 36% equally divided amongst the enthalpy fluxes of the suprathermal protons, alphas, and electrons.
6. Those enthalpy fluxes are somewhat offset by the upstream-directed thermal and suprathermal heat fluxes which together carry 21% of the net total energy flux back toward the upstream region.
7. The downstream Poynting flux carries ∼10% of the total energy flux.

Comparing these remarks with the two quasi-perpendicular shocks studied in Sch22 (see, e.g., Figures 1, 4i, and 4j of that paper) reveals that this quasi-parallel shock has incident and downstream energy fluxes distributed in a more complex way. Less of the incident energy flux is in simple ram energy (85% here vs. 94%) with upstream enthalpy and heat fluxes contributing both more flux and competing upstream-directed fluxes. The alpha particles also play a larger role here.

Downstream, this quasi-parallel shock converts a similar amount of energy flux into thermal (47%) and suprathermal (12%) protons compared to 61% in the quasi-perpendicular case. Much more ram energy survives (24% in total vs. ≤10%). The downstream also shows competing upstream-directed heat fluxes that are absent in the quasi-perpendicular case. The shocks in Sch22 are slightly higher in Mach number (∼6 there vs. 4.6 here).

The shaded interval in Figure 3 shows a particularly dramatic departure from constant total energy flux (gold trace in (i)). The drop to essentially zero ram pressure could be the result of significant shock motion relative to the spacecraft frame. Although multi-spacecraft timing techniques are difficult to apply here, we have attempted to determine the motion of individual "crossings" during this interval by imposing proton flux continuity. This addresses part of the time dependence of the shock motion, although not its orientation, provided that the underlying temporal change is longer than the individual crossing and that the corresponding upstream and downstream conditions have settled into a new quasi-steady state.

For a given crossing, we apply a least squares analysis of the normal proton flux conservation equation $n_p\left(u'_n - V_n^{sh}\right) = \text{const}$ to determine the unknown shock motion V_n^{sh}. The fluctuations and probably real unsteady motion can render the result inaccurate, to the extent that the solutions for some of the crossings even have the wrong sense of motion by comparison to the observed crossing traversal. The shaded crossing yields a rather large value of $V_n^{sh} \approx +160$ km/s.

We have recalculated the energy fluxes for the shaded interval using this shock motion to estimate the fluxes in the shock rest frame. The results are shown in the set of panels to the right in Figure 3. Panels (d')–(h') have been rescaled to accommodate the larger energy fluxes, but they all cover the same total range. There is still a significant but reduced lack of constancy in the total energy flux (gold trace in panel (i')) but now all the enthalpy fluxes (panel (e')) rise together toward the downstream. Even this dramatic attempt to explore the time variations of the shock does not drastically alter the relative partition of energy seen in the spacecraft frame fluxes in Panels (d–i). Panel (a') also shows the improvement in background at low energies in the FPI burst data products compared to the fast survey data used to set continuous context. We use burst data for all our flux calculations and proton partial moments.

6. Suprathermal and Energetic Particles

Figure 4 compares the FPI thermal (<4 keV) and suprathermal (4−32 keV) ion (assumed to be dominated by protons) sub-populations together with the EIS energetic (31–80 keV) protons. In the absence of a velocity moment from EIS, we have calculated the enthalpy flux (panel (e)) of the energetic protons by combining their assumed isotropic pressure (blue in panel (d)) with the bulk velocity (panel (b)) of the suprathermal protons. We have calculated the energetic proton contributions from the full resolution data, and show in Figure 4 smoothed versions that remove the spintone inherent in the original data. We also show a smoothed version of the suprathermal proton normal velocity (panel (b)).

Perhaps the most noteworthy aspect of Figure 4 is the near constancy of both the suprathermal and energetic proton densities and their pressures despite the four distinct shock-like transitions shown in the figure. The systematic velocity variations still give rise to some changes in enthalpy flux for these components, but it is less pronounced and, of course, smaller in magnitude compared to the thermal component. The picture here is of an extended region bathed in a sea of suprathermal and energetic protons, for which the location relative to a shock-like transition makes little impact.

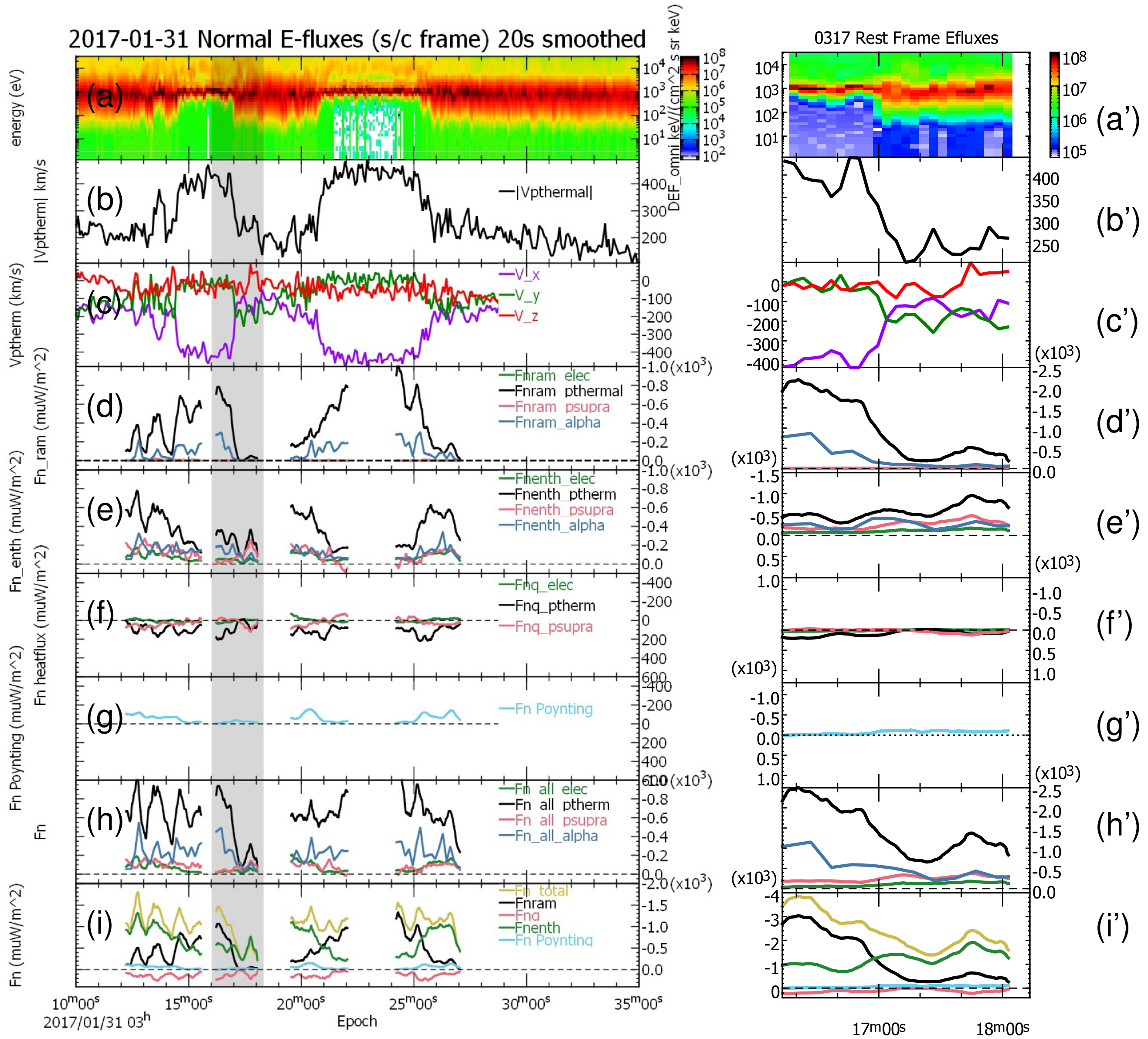

Figure 3. Energy fluxes for the period 03:10 to 03:35, in the same format as Figure 2. The left set of panels are just an expanded version of the same fluxes in Figure 2 as measured in the spacecraft frame. The right set of panels recalculate those energy fluxes for the shaded interval by moving into a local shock rest frame. The ranges for panels (d'–h') are all the same, but expanded relative to those in panels (d–h).

7. Energy Fluxes Carried by Fluctuations

In Sch22 we developed an approach to calculate energy fluxes associated with fluctuations in both plasma and field parameters. Large-amplitude fluctuations and wave fields are a universal feature of quasi-parallel shocks. The approach is straightforward. First, up to now we have employed full resolution measurements of all the plasma and field parameters X_k (i.e., ρ_j, $\mathbf{u}_j'$, p_j, $\mathbf{q}_j$ for all the species j together with $\mathbf{E}$ and $\mathbf{B}$) to calculate the normal component of the various energy fluxes derived in Section 3, that is, $F_n(X_1, X_2, \dots)$. These will include any fluxes associated with parameter fluctuations up to the sampling frequency of the instrumentation. Fluctuation contributions arise due to the nonlinear nature of the expressions for the different energy fluxes.

The fluxes with fluctuation contributions removed can be calculated by first smoothing the underlying data parameters X_k. This smoothing is simply a running averaging process, which we can denote as $\langle .. \rangle_t$. We then

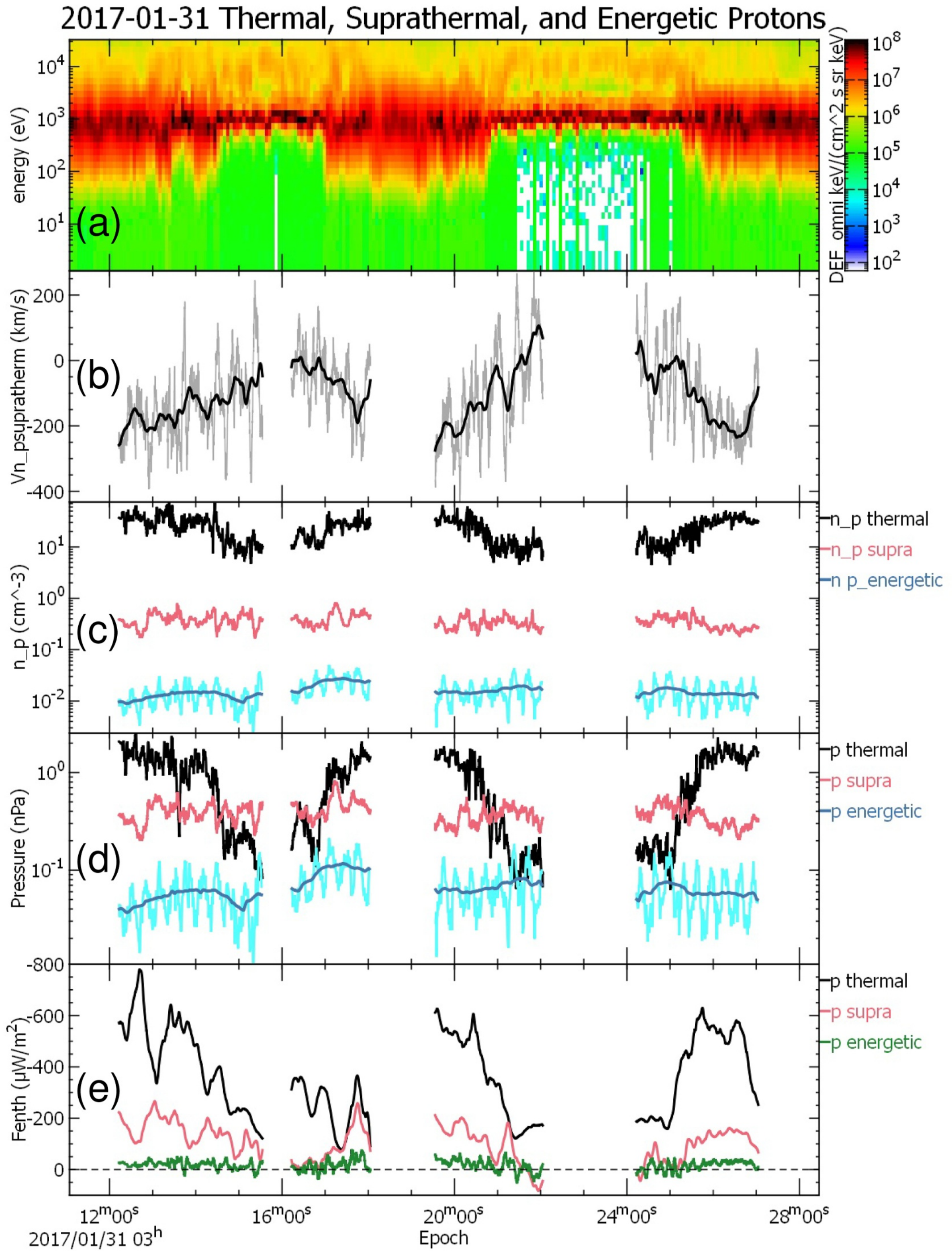

Figure 4. Relative contributions of the different proton sub-populations. (a) Fast Plasma Investigation (FPI) ion differential energy flux spectrogram for context. (b) Normal component of the bulk velocity of the suprathermal (4–32 keV) protons from FPI. Densities (c) and pressures (d) of the three sub-populations. Panel (e) shows the normal component of the enthalpy fluxes carried by these sub-populations in the spacecraft frame. Light gray (c) or blue (d) traces are the full resolution products, on which smoothed dark traces are overlain.

calculate the energy fluxes $F_n\left(\langle X_1\rangle_t, \langle X_2\rangle_t, \dots\right)$ using those smoothed parameters. The difference between these two calculations of fluxes provides the fluxes carried by fluctuations, that is,

$$F_n^{fluctuations} = F_n(X_1, X_2, \dots) - F_n\left(\langle X_1\rangle_t, \langle X_2\rangle_t, \dots\right) \tag{9}$$

This process is cleaner than expanding all the expressions for the F_n's in terms of unsmoothed and smoothed parameters, for example, by writing $\delta X_k = X_k - \langle X_k\rangle_t$ and then trying to collect the nonlinear terms in the different F_n's.

In Figures 2 and 3, we have shown smoothed versions of $F_n(X_1, X_2, \dots)$. Since those F_n are smoothed after calculating the fluxes, they retain the systematic contributions from any fluctuations present in the data.

Figure 5 shows that relatively little energy is carried by fluctuations in particle moments. The ram energy flux (panel (b)) shows the largest and most frequent deviations, with the fluxes from the full resolution data being larger in magnitude by up to 100 μW/m^2. These differences all occur in downstream or indeterminate regions (e.g., near 03:13:30). The ram energy is the flux that is of highest multiplicative order, which may be responsible for the enhanced sensitivity to fluctuations. The proton enthalpy fluxes (panels (c) and (d)) show smaller differences, with one or two for which the fluxes from pre-smoothed parameters are actually larger than the smoothed $F_n(\text{fullres})$ (e.g., also at 03:13:30 and at 03:17:00). Other fluxes not shown in the figure show smaller differences than those shown.

Although the energy fluxes associated with the particle populations have minor contributions from fluctuations, that is not the case for the Poynting flux shown in Figure 5e. Pre-smoothing the field data with a 20 s window leaves almost zero Poynting flux. The highly variable Poynting flux (light blue trace) has a persistent (dark blue trace), downstream-directed energy flux in the downstream regions of ∼10% of the total energy flux. That flux is therefore carried by fluctuations in the fields on scales shorter than 20s, up to the magnetic field sampling frequency of 128 Hz. Wilson et al. (2014) reported large (up to 2000 μW/m^2) Poynting fluxes associated with high frequency (>10 Hz) waves localized to regions of sharp magnetic gradients. These waves exchange energy with the particle populations as part of the detailed shock dissipation mechanisms. The net energy exchange will appear here in the macroscopic particle energy fluxes, with the residual Poynting flux representing a real component of the total energy flux in the downstream regions.

8. Summary

From Figures 3 and 4 we can extract typical values of all the normal fluxes in the upstream and downstream regions. Given the variability from one transition crossing to another, and the fluctuations within each crossing, these are crude estimates that serve to order and compare the relative contributions. Figures 6a and 6b provides a summary of these fluxes based on the relatively simple transition at 03:21. In Panels (c) and (d) we have recast the results for the quasi-perpendicular shock on 05-03-2019 studied in detail in Sch22.

Some key observations emerge from Figure 6:

1. Roughly half of the total energy flux in the shocked regions is carried by the enthalpy flux of the thermal (<4 keV) protons. A fifth of the total is carried mainly by residual proton ram energy with a further 5% in residual alpha particle ram energy.
2. The total proton enthalpy flux upstream (downstream) is offset 50% (34%) by upstream-directed proton heat fluxes. These may be best interpreted as manifestations of distortions in phase space density distributions present both up- and downstream.
3. The suprathermal (4–32 keV) and energetic (31–80 keV) protons show little variation in density across the extended region (Figure 4) and only small variations in the enthalpy flux they carry.
4. The suprathermal protons represent 1% of the total population, and carry 12% of the total downstream proton enthalpy plus heat fluxes.
5. Only a small number of more energetic (32–80 keV) protons are present, but these carry 9% of the total downstream proton enthalpy plus heat fluxes.

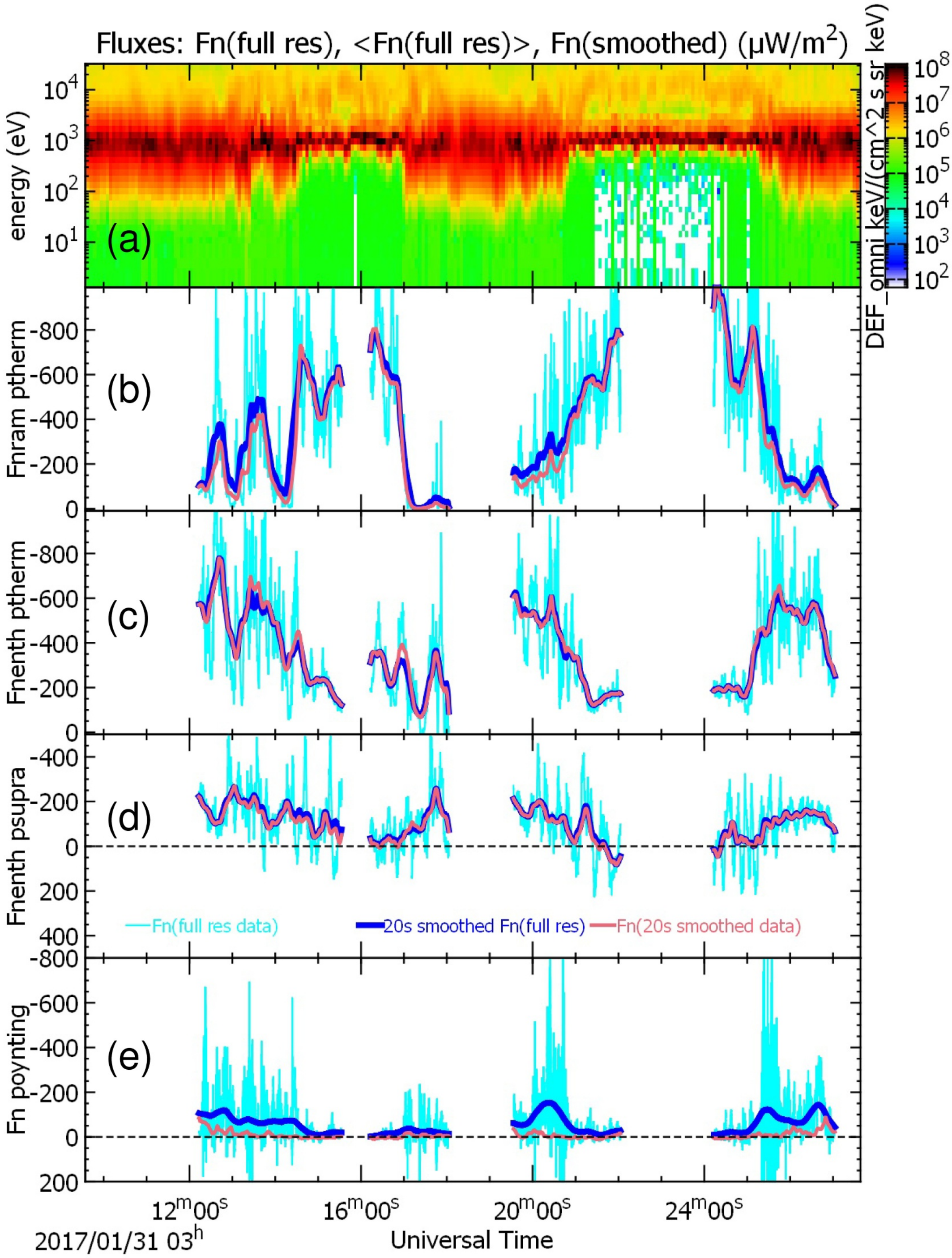

Figure 5. Energy fluxes with/without fluctuations, for the same interval as in Figure 3. Fast Plasma Investigation differential energy flux spectrogram (a) for context. Subsequent panels show a subset of energy fluxes calculated from the full resolution data (light blue), 20s smoothed versions of those full fluxes (dark blue) as shown in previous figures, and fluxes calculated from 20s smoothed parameter values (pink). Shown are the ram (b) and enthalpy (c) fluxes carried by the thermal protons, the enthalpy flux (d) carried by the suprathermal protons, and (e) the Poynting flux. All flux panels span the same range of values, with inverted scales as in previous figures.

(a)

Flux type/Carrier	Up	Down
Ram energy flux		
Thermal protons	-730	-200
Suprath protons	0	0
Alpha particles	-130	-50
Electrons	0	0
Total Ram E-Flux	-860	-250
Enthalpy flux		
Thermal protons	-150	-500
Suprath protons	+50	-130
Alpha particles	-50	-130
Electrons	-50	-130
Energetic protons	0	-40
Total Enthalpy Flux	-200	-930
Heatflux		
Thermal protons	+100	+150
Suprath protons	-50	+75
Alpha particles	0	0
Electrons	0	0
Total Heat Flux	+50	+225
Poynting Flux	0	-100
Grand Totals	-1010	-1055

(c)

Flux type/Carrier	Up	Down
Ram energy flux		
Thermal protons	-175.4	-17.2
Non-core protons	0	0
Alpha particles	-3.7	-0.3
Electrons	0	0
Total Ram E-Flux	-179.1	–17.5
Enthalpy flux		
Thermal protons	-4.3	-48.8
Non-core protons	0	-71.3
Alpha particles	-0.1	-2.4
Electrons	-3.2	-33
Total Enthalpy Flux	-7.6	-155.5
Heatflux		
Thermal protons	0	-3.2
Noncore protons	0	0
Alpha particles	0	0
Electrons	0	0
Total Heat Flux	0	-3.2
Poynting Flux	-6.2	-21.0
Grand Totals	-192.9	-197.2

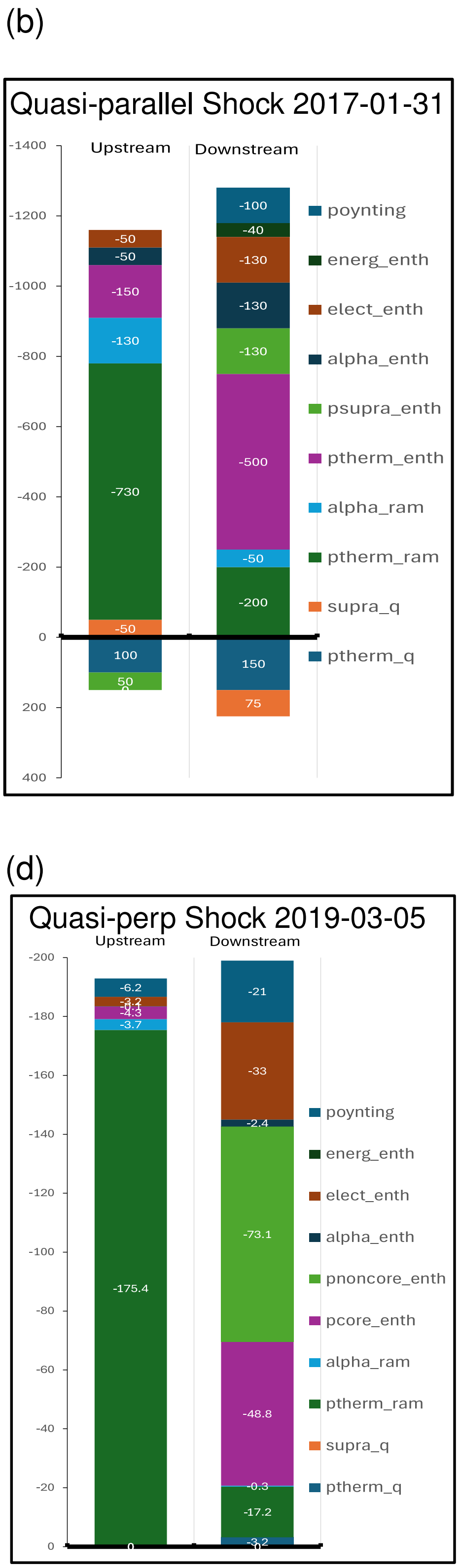

Figure 6. Energy fluxes in μW/m^2 by type and carrier. The top panels show (a) tabulated values and (b) stacked bar charts for the quasi-parallel shock studied here evaluated near 03:21. The bottom panels show in the same format values from the quasi-perpendicular shock studied in Sch22 for comparison.

6. In terms of the net shock energy flux of $\sim 1030 \mu\mathrm{W/m}^2$, the suprathermal net contribution is 5% and the energetic particles contribute 4%, so the total nonthermal protons carry 9% of the downstream energy flux. This is consistent with the fraction reported by David et al. (2022) at interplanetary shocks.
7. The Poynting flux carries 10% of the total downstream energy flux. That flux is entirely related to fluctuations with periods less than 20 s. This is different from the quasi-perpendicular case where there is a quasi-static Poynting flux.

In the quasi-perpendicular case of Sch22 (see, e.g., Figure 3 of that paper recast and extended where possible here in Figure 6d) a significant amount (60%) of the proton enthalpy flux is carried by the 20% of protons residing outside of the core population, delineated in Sch22 by a region in 3D velocity space. However, that non-core population reached energies that only marginally exceeded the incident bulk flow energy. Here, the quasi-parallel shock accelerates a small number of protons to much higher energies, such that 21% of the combined proton enthalpy and heat flux is carried by just 1% of the protons.

The two cases also display differences in the input and residual ram energy. In the quasi-perpendicular shock, 93% of the incident energy flux was carried as ram energy, and only 9% of the downstream energy flux remained as ram energy. Here, the quasi-parallel case has 85% of its incident energy flux as ram energy, with more significant contributions from the enthalpy and heat fluxes due mainly to the shock-related suprathermal particles. In the downstream region, 25% of the total energy flux remains as ram energy. Part of this difference may be due to the higher Mach number in the quasi-perpendicular case studied in Sch22 (5.6 compared to 4.6 in this work). However, the one-fluid ($\gamma = 5/3$) Rankine Hugoniot jump conditions predict that the ratio of downstream to upstream ram energy for both cases is 0.25. This prediction is not far off the observational value (0.29) here, but the quasi-perpendicular case leaves only one tenth of the ram energy surviving into the downstream region. Further examples will be needed to establish whether this difference is systematic, and, if so, why.

The time series of energy fluxes shown in several of the figures here highlights the variability of both the plasma parameters and resulting energy fluxes. Once fluctuations shorter than 20 s have been removed, most of the energy fluxes show clear trends across shock-like transitions despite variations of 10%–30% or more. The total energy flux is somewhat less variable, suggesting that there are intrinsic variations in the way that energy is partitioned. Importantly, none of those variations re-order the different energy fluxes, so there remains a clear ranking in terms of size. Further examples are needed to explore the quantitative ranking of, for example, energy being partitioned into energetic particles, as a function of upstream conditions.

9. Conclusions

Collisionless shocks partition the incident energy in ways that have only recently begun to be addressed in a meaningful way (David et al., 2022; Schwartz et al., 2022). It impacts not only the main heating of, for example, protons and electrons, but also the generation of turbulence, the acceleration of sub-populations of particles, and the kinetics of the minor species. Here we have applied a framework for organizing the various energy fluxes to the case of a shock at which the upstream magnetic field is nearly parallel to the shock normal. Unlike the relatively stable, more laminar quasi-perpendicular shock, particle transport along the field yields a highly turbulent, non-steady and extended transition often accompanied by suprathermal and more highly energized particles.

We were able to evaluate the ram, enthalpy, and heat fluxes associated with thermal, suprathermal and energetic protons together with the alpha particle and electron contributions and the Poynting flux using high quality in situ data at the Earth's bow shock measured by MMS. During the quasi-parallel interval presented in this paper, the suprathermal (4–32 keV) and energetic (>32 keV) protons form a sea of particles that vary only a little across transitions that otherwise look like shock crossings. Nonetheless, those variations are sufficient to result in a significant take up of energy flux in the downstream regions, accounting for nearly 10% of the overall shock energy flux. We should note that we have concentrated here on relatively local, clear transitions. The plasma upstream of those transitions already contain products of shock processes including suprathermal ions. We have not addressed the full transition from pristine solar wind far upstream to far downstream, that is, treating the extended foreshock region as part of the shock, although the parameter values in Table 1 correspond to those pristine conditions.

We also studied fluctuations in the plasma parameters and the extent to which those fluctuations represented additional contributions to the energy flux on either side of the shock. We found some evidence for some impact on the ram energy fluxes. Additionally, the systematic Poynting flux is carried by fluctuations with periods less than 20s; there is no significant Poynting flux associated with the DC electric and magnetic fields. Taken together, the fluctuations carry 10%–20% of the total energy flux in the downstream regions. This energy flux would be ignored in studies that average the plasma and field parameters over intervals representative of the upstream and downstream states.

Qualitatively, parameters at quasi-parallel shocks are highly variable. Interestingly, we found that after removing fluctuations in energy fluxes shorter than 20 s the resulting energy fluxes showed systematic trends across shock-like transitions. The residual fluctuations in those energy fluxes, while large, did not change the relative size of the contributions of the dominant energy carriers.

The present work complements the statistical study of energetic particles at interplanetary shocks by David et al. (2022) which focussed on the jump in fluxes averaged either side of rapidly propagating shocks, and on very energetic particles in the downstream region. Our more detailed observations by MMS probe the variability of the nearly standing terrestrial bow shock under turbulent, quasi-parallel conditions. While David et al. (2022) find that shocks of all field orientations are associated with energetic particles, that is not the case at the bow shock. The difference probably lies in the large time and length scales available to interplanetary shocks. Thus studying the terrestrial bow shock sheds complementary light on, for example, stages in the production of energetic particles.

Studies of quasi-parallel shocks present significant challenges, both due to their observational complexity and the underlying physics. Our methodology assumed, for example, that the shock normal was constant and prescribed by an empirical bow shock model. The fluctuating fields, non-steady shock motion, and finite-sized structures remain to be characterized with sufficient clarity to enable spacecraft observations to be cast into that more complicated time-dependent nonplanar environment. Additionally, resolving the narrow solar wind proton and alpha beams while also covering the full 4π velocity space needed for the shocked magnetosheath plasma downstream of the Earth's bow shock is challenging. Future missions could address some of these limitations by targetted instrumentation in near-Earth space (Goodrich et al., 2023). Traveling interplanetary shocks (e.g., David et al. (2022)) have the advantage that the shocked state still has a relatively narrow solar wind beam, but the challenge is to resolve it fast enough and with sufficient resolution.

Appendix A: Details

Figure A1 shows the full resolution version of Figure 2.

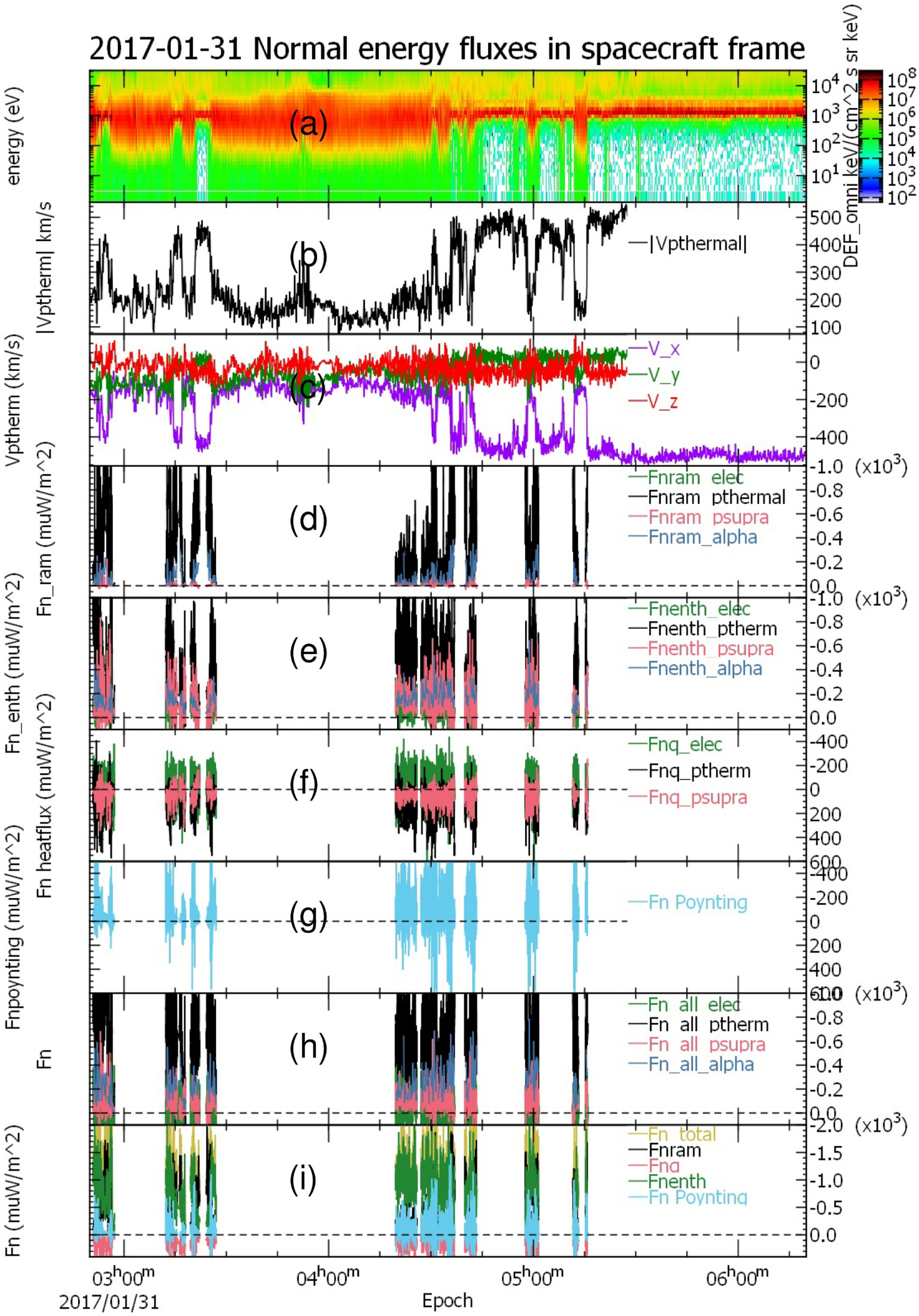

Figure A1. Same as Figure 2 from main paper but with unsmoothed energy fluxes calculated from the full resolution data.

Conflict of Interest

The authors declare no conflicts of interest relevant to this study.

Data Availability Statement

Wind data were drawn from the SPDF/CDAWEB repository (https://cdaweb.gsfc.nasa.gov/index.html/) under Wind→WI_H2_MFI (Koval & Szabo, 2021), →WI_PLSP_3DP (Lin, Bale, Wilson III, & Schroeder, 2021), and →WI_ELM2_3DP (Lin, Bale, & Wilson III, 2021). THEMIS data (THEMIS Instrument Teams, 2007-2026; Angelopoulos, 2008) were drawn from the SPDF/CDAWEB repository (https://cdaweb.gsfc.nasa.gov/index.html/) under THEMIS→ THC_L2_FGM. MMS data (MMS Science Data Center and Instrument Teams, 2015-2026) can be found at the MMS public Science Data Center (https://lasp.colorado.edu/mms/sdc/public/search) by completing the search form for the appropriate date/time, instrument and data rate as described in Section 2. Fast FPI survey data is found under "fast" data rate.

Software: Data analysis and graphics were performed using the opensource QSAS Science Analysis System (https://sourceforge.net/projects/qsas/) version 3.4.1 (QSAS teams, 1990-2025). QSAS savesets for this work, which contain subsets of the data found in the repositories listed in the previous subsection and derived products, QSASCalculator analysis pages, and graphical routines are available at zenodo.org (Schwartz, 2026).

Acknowledgments

We gratefully acknowledge the respective instrument teams and archive curators. This work was supported by NASA MMS contracts to the instrument teams. SR acknowledges funding from the MMS Early Career Award 80NSSC25K7353. QSAS software used here was developed over many years by teams at Queen Mary University of London and Imperial College London with the support of the UK Science and Technology Facilities Council and its predecessors. We are grateful for the personal support and maintenance of QSAS in recent years by Dr. Tony Allen.

References

Amano, T., Katou, T., Kitamura, N., Oka, M., Matsumoto, Y., Hoshino, M., et al. (2020). Observational evidence for stochastic shock drift acceleration of electrons at the Earth's bow shock. *Physical Review Letters*, *124*(6), 065101. https://doi.org/10.1103/PhysRevLett.124.065101

Angelopoulos, V. (2008). The THEMIS Mission. *Space Science Reviews*, *141*(1–4), 5–34. https://doi.org/10.1007/s11214-008-9336-1

Balikhin, M. A., Gedalin, M., Walker, S. N., Agapitov, O. V., & Zhang, T. (2023). Structure of a quasi-parallel shock front. *The Astrophysical Journal*, *959*(2), 130. https://doi.org/10.3847/1538-4357/ad0b71

Burch, J. L., Moore, T. E., Torbert, R. B., & Giles, B. L. (2016). Magnetospheric multiscale overview and science objectives. *Space Science Reviews*, *199*(1–4), 5–21. https://doi.org/10.1007/s11214-015-0164-9

Burgess, D., & Scholer, M. (2015). *Collisionless shocks in space plasmas*. Cambridge University Press.

David, L., Fraschetti, F., Giacalone, J., Wimmer-Schweingruber, R. F., Berger, L., & Lario, D. (2022). In situ measurement of the energy fraction in suprathermal and energetic particles at ACE, wind, and PSP interplanetary shocks. *Astrophysical Journal*, *928*(1), 66. https://doi.org/10.3847/1538-4357/ac54af

Ergun, R. E., Tucker, S., Westfall, J., Goodrich, K. A., Malaspina, D. M., Summers, D., et al. (2016). The axial double probe and fields signal processing for the MMS Mission. *Space Science Reviews*, *199*(1–4), 167–188. https://doi.org/10.1007/s11214-014-0115-x

Gedalin, M. (2020). Large-scale versus small-scale fields in the shock front: Effect on the particle motion. *Astrophysical Journal*, *895*(1), 59. https://doi.org/10.3847/1538-4357/ab8af0

Gingell, I., Schwartz, S. J., Eastwood, J. P., Burch, J. L., Ergun, R. E., Fuselier, S., et al. (2019). Observations of magnetic reconnection in the transition region of quasi-parallel shocks. *Geophysical Research Letters*, *46*(3), 1177–1184. https://doi.org/10.1029/2018GL081804

Gingell, I., Schwartz, S. J., Eastwood, J. P., Stawarz, J. E., Burch, J. L., Ergun, R. E., et al. (2020). Statistics of reconnecting current sheets in the transition region of earth's bow shock. *Journal of Geophysical Research*, *125*(1), e27119. https://doi.org/10.1029/2019JA027119

Golan, M., & Gedalin, M. (2025). Observations of persistent downstream magnetic oscillations at the earth bow shock. *Journal of Geophysical Research: Space Physics*, *130*(9), e2025JA034321. https://doi.org/10.1029/2025ja034321

Gomez, R. G., Fuselier, S. A., Mukherjee, J., Gonzalez, C. A., Burch, J. L., Strangeway, R. J., & Starkey, M. J. (2019). The extra-magnetospheric ion environment as observed by the magnetospheric Multiscale Mission hot plasma composition analyzer (MMS-HPCA). *Journal of Geophysical Research*, *124*(3), 1509–1524. https://doi.org/10.1029/2018JA025392

Goodrich, K., Cohen, I. J., Schwartz, S., Wilson, L. B., Turner, D., Caspi, A., et al. (2023). The multi-point assessment of the kinematics of shocks (MAKOS). *Frontiers in Astronomy and Space Sciences*, *10*, 1199711. https://doi.org/10.3389/fspas.2023.1199711

Goodrich, K. A., Ergun, R., Schwartz, S. J., Wilson, L. B., Newman, D., Wilder, F. D., et al. (2018). MMS observations of electrostatic waves in an oblique shock crossing. *Journal of Geophysical Research*, *123*(11), 9430–9442. https://doi.org/10.1029/2018JA025830

Harten, R., & Clark, K. (1995). The design features of the GGS wind and polar spacecraft. *Space Science Reviews*, *71*(1–4), 23–40. https://doi.org/10.1007/BF00751324

Johlander, A., Battarbee, M., Turc, L., Ganse, U., Pfau-Kempf, Y., Grandin, M., et al. (2022). Quasi-Parallel shock reformation seen by Magnetospheric Multiscale and ion-kinetic simulations. *Geophysical Research Letters*, *49*(2), e96335. https://doi.org/10.1029/2021GL096335

Johlander, A., Vaivads, A., Khotyaintsev, Y. V., Gingell, I., Schwartz, S. J., Giles, B. L., et al. (2018). Shock ripples observed by the MMS spacecraft: Ion reflection and dispersive properties. *Plasma Physics and Controlled Fusion*, *60*(12), 125006. https://doi.org/10.1088/1361-6587/aae920

Kang, H., & Jones, T. W. (2007). Self-similar evolution of cosmic-ray-modified quasi-parallel plane shocks. *Astroparticle Physics*, *28*(2), 232–246. https://doi.org/10.1016/j.astropartphys.2007.05.007

Kis, A., Scholer, M., Klecker, B., Möbius, E., Lucek, E. A., Rème, H., et al. (2004). Multi-spacecraft observations of diffuse ions upstream of Earth's bow shock. *Geophysical Research Letters*, *31*(20), L20801. https://doi.org/10.1029/2004GL020759

Koval, A., & Szabo, A. (2021). Wind magnetic field investigation (mfi) data at full resolution [Dataset]. *NASA Space Physics Data Facility*. https://doi.org/10.48322/0V0H-DF27

Krasnoselskikh, V., Balikhin, M., Walker, S. N., Schwartz, S. J., Sundkvist, D., Lobzin, V., et al. (2013). The dynamic quasiperpendicular shock: Cluster discoveries. *Space Science Reviews*, *178*(2–4), 535–598. https://doi.org/10.1007/s11214-013-9972-y

Kucharek, H., Möbius, E., Li, W., Farrugia, C. J., Popecki, M. A., Galvin, A. B., et al. (2003). On the source and acceleration of energetic He^+: A long-term observation with ACE/SEPICA. *Journal of Geophysical Research*, *108*(A10), 8040. https://doi.org/10.1029/2003JA009938

Kucharek, H., Möbius, E., Scholer, M., Mouikis, C., Kistler, L., Horbury, T., et al. (2004). On the origin of field-aligned beams at the quasi-perpendicular bow shock: Multi-spacecraft observations by Cluster. *Annals of Geophysics*, *22*(7), 2301–2308. https://doi.org/10.5194/angeo-22-2301-2004

Leroy, M. M., Winske, D., Goodrich, C. C., Wu, C. S., & Papadopoulos, K. (1982). The structure of perpendicular bow shocks. *Journal of Geophysical Research*, *87*(A7), 5081–5094. https://doi.org/10.1029/JA087iA07p05081

Lin, R. P., Bale, S. D., & Wilson III, L. B. (2021). Wind 3dp eesa-low electron moments [Data]. *NASA Space Physics Data Facility; Space Sciences Laboratory*. University of California Berkeley. https://doi.org/10.48322/4TK0-A011

Lin, R. P., Bale, S. D., Wilson III, L. B., & Schroeder, P. (2021). Wind 3dp 24-sec ion omnidirectional fluxes and moments. *NASA Space Physics Data Facility*; Space Sciences Laboratory, University of California Berkeley [Data]. https://doi.org/10.48322/C4MF-9N52

Lindqvist, P.-A., Olsson, G., Torbert, R. B., King, B., Granoff, M., Rau, D., et al. (2016). The spin-plane double probe electric field instrument for MMS. *Space Science Reviews*, *199*(1–4), 137–165. https://doi.org/10.1007/s11214-014-0116-9

Longmore, M. M. (2005). *Multi-spacecraft observations at earth's bow shock and a survey of the dayside magnetosheath* (*PhD*, Queen Mary University of London). Retrieved from https://search.library.qmul.ac.uk/iii/encore/record/C__Rb1304326 (Chapter 6)

Madanian, H., Desai, M. I., Schwartz, S. J., Wilson, I. L. B., Fuselier, S. A., Burch, J. L., et al. (2021). The dynamics of a high Mach number quasi-perpendicular shock: MMS observations. *Astrophysical Journal*, *908*(1), 40. https://doi.org/10.3847/1538-4357/abcb88

Mauk, B. H., Blake, J. B., Baker, D. N., Clemmons, J. H., Reeves, G. D., Spence, H. E., et al. (2016). The Energetic Particle Detector (EPD) investigation and the Energetic Ion Spectrometer (EIS) for the magnetospheric Multiscale (MMS) Mission. *Space Science Reviews*, *199*(1–4), 471–514. https://doi.org/10.1007/s11214-014-0055-5

MMS Science Data Center and Instrument Teams. (2015-2026). MMS public data [Data]. *MMS Science Data Center*. Retrieved from https://lasp.colorado.edu/mms/sdc/public/

Park, J., Caprioli, D., & Spitkovsky, A. (2015). Simultaneous acceleration of protons and electrons at nonrelativistic quasiparallel collisionless shocks. *Physical Review Letters*, *114*(8), 085003. https://doi.org/10.1103/PhysRevLett.114.085003

Paschmann, G., Sckopke, N., Bame, S. J., & Gosling, J. T. (1982). Observations of gyrating ions in the foot of the nearly perpendicular bow shock. *Geophysical Research Letters*, *9*(8), 881–884. https://doi.org/10.1029/GL009i008p00881

Plank, J., & Gingell, I. (2023). Intermittency at earth's bow shock: Measures of turbulence in quasi-parallel and quasi-perpendicular shocks. *Physics of Plasmas*, *30*(8), 082906. https://doi.org/10.1063/5.0160439

Pollock, C., Moore, T., Jacques, A., Burch, J., Gliese, U., Saito, Y., et al. (2016). Fast plasma investigation for Magnetospheric Multiscale. *Space Science Reviews*, *199*(1–4), 331–406. https://doi.org/10.1007/s11214-016-0245-4

QSAS teams. (1990-2025). QSAS science analysis software for space plasmas. Version 3.4.1 [Software]. Queen Mary University of London and Imperial College London. Retrieved from https://sourceforge.net/projects/qsas

Raptis, S., Karlsson, T., Vaivads, A., Pollock, C., Plaschke, F., Johlander, A., et al. (2022). Downstream high-speed plasma jet generation as a direct consequence of shock reformation. *Nature Communications*, *13*(1), 598. https://doi.org/10.1038/s41467-022-28110-4

Russell, C. T., Anderson, B. J., Baumjohann, W., Bromund, K. R., Dearborn, D., Fischer, D., et al. (2016). The Magnetospheric Multiscale magnetometers. *Space Science Reviews*, *199*(1–4), 189–256. https://doi.org/10.1007/s11214-014-0057-3

Schwartz, S. (2026). Qsas savesets repository for energy partition at a collisionless supercritical quasi-parallel shock [ComputationalNotebook]. *Zenodo*. https://doi.org/10.5281/zenodo.18267662

Schwartz, S. J. (1991). Magnetic field structures and related phenomena at quasi-parallel shocks. *Advances in Space Research*, *11*(9), 231–240. https://doi.org/10.1016/0273-1177(91)90039-M

Schwartz, S. J. (1998). Shock and discontinuity normals, Mach numbers, and related parameters. *ISSI Scientific Reports Series*, *1*, 249–270.

Schwartz, S. J. (2006). Shocks: Commonalities in solar-terrestrial chains. Sp. *Science Review*, *124*(1–4), 333–344. https://doi.org/10.1007/s11214-006-9093-y

Schwartz, S. J., & Burgess, D. (1991). Quasi-parallel shocks: A patchwork of three-dimensional structures. *Geophysical Research Letters*, *18*(3), 373–376. https://doi.org/10.1029/91GL00138

Schwartz, S. J., Burgess, D., Wilkinson, W. P., Kessel, R. L., Dunlop, M., & Luehr, H. (1992). Observations of short large-amplitude magnetic structures at a quasi-parallel shock. *Journal of Geophysical Research*, *97*(A4), 4209–4227. https://doi.org/10.1029/91JA02581

Schwartz, S. J., Ergun, R., Kucharek, H., Wilson, L., Chen, L.-J., Goodrich, K., et al. (2021). Evaluating the deHoffmann-Teller cross-shock potential at real collisionless shocks. *Journal of Geophysical Research*, *126*(8), e29295. https://doi.org/10.1029/2021JA029295

Schwartz, S. J., Goodrich, K. A., Wilson, L. B., Turner, D. L., Trattner, K. J., Kucharek, H., et al. (2022). Energy partition at Collisionless supercritical quasi-perpendicular shocks. *Journal of Geophysical Research (Space Physics)*, *127*(10), e2022JA030637. https://doi.org/10.1029/2022JA030637

Schwartz, S. J., Thomsen, M. F., Bame, S. J., & Stansberry, J. (1988). Electron heating and the potential jump across fast mode shocks. *Journal of Geophysical Research*, *93*(A11), 12923–12931. https://doi.org/10.1029/JA093iA11p12923

Schwartz, S. J., Zweibel, E. G., & Goldman, M. (2013). Microphysics in astrophysical plasmas. Sp. *Science Review*, *178*(2–4), 81–99. https://doi.org/10.1007/s11214-013-9975-8

Sckopke, N., Paschmann, G., Bame, S. J., Gosling, J. T., & Russell, C. T. (1983). Evolution of ion distributions across the nearly perpendicular bow shock: Specularly and non-specularly reflected-gyrating ions. *Journal of Geophysical Research*, *88*(A8), 6121–6136. https://doi.org/10.1029/JA088iA08p06121

Scudder, J. D., Mangeney, A., Lacombe, C., Harvey, C. C., & Aggson, T. L. (1986). The resolved layer of a collisionless, high β, supercritical, quasi-perpendicular shock wave. 2. Dissipative fluid electrodynamics. *Journal of Geophysical Research*, *91*(A10), 11053–11074. https://doi.org/10.1029/JA091iA10p11053

Scudder, J. D., Mangeney, A., Lacombe, C., Harvey, C. C., Wu, C. S., & Anderson, R. R. (1986). The resolved layer of a collisionless, high β, supercritical, quasi-perpendicular shock wave, 3. Vlasov electrodynamics. *Journal of Geophysical Research*, *91*(A10), 11075–11098. https://doi.org/10.1029/JA091iA10p11075

Slavin, J. A., & Holzer, R. E. (1981). Solar wind flow about the terrestrial planets, 1. Modeling bow shock position and shape. *Journal of Geophysical Research*, *86*(A13), 11401–11418. https://doi.org/10.1029/JA086iA13p11401

Stone, R. G., & Tsurutani, B. T. (1985). Collisionless shocks in the heliosphere. A tutorial review. *Washington DC American Geophysical Union Geophysical Monograph Series*, *34*. https://doi.org/10.1029/GM034

THEMIS Instrument Teams. (2007-2026). THEMIS data repository [Data]. *NASA Space Physics Data Facility*. Retrieved from https://cdaweb.gsfc.nasa.gov/index.html

Torbert, R. B., Russell, C. T., Magnes, W., Ergun, R. E., Lindqvist, P.-A., LeContel, O., et al. (2016). The FIELDS instrument suite on MMS: Scientific objectives, measurements, and data products. *Space Science Reviews*, *199*(1–4), 105–135. https://doi.org/10.1007/s11214-014-0109-8

Toy Edens, V., Raptis, S., Turner, D. L., Mo, W., & Young, S. A. Q. (2025). Automated bow shock identification and multi spacecraft timing using magnetospheric Multiscale (MMS) observations. *Journal of Geophysical Research (Space Physics)*, *130*(10), e2025JA034252. https://doi.org/10.1029/2025JA034252

Trattner, K. J., Fuselier, S. A., Schwartz, S. J., Kucharek, H., Burch, J. L., Ergun, R. E., et al. (2023). Ion acceleration at the quasi-parallel shock: The source distributions of the diffuse ions. *Journal of Geophysical Research (Space Physics)*, *128*(2), e2022JA030631. https://doi.org/10.1029/2022JA030631

Tsurutani, B. T., & Stone, R. G. (1985). Collisionless shocks in the heliosphere: Reviews of current research. *Washington DC American Geophysical Union Geophysical Monograph Series*, *35*. https://doi.org/10.1029/GM035

Wang, S., Chen, L.-J., Bessho, N., Hesse, M., Wilson, L. B., Giles, B., et al. (2019). Observational evidence of magnetic reconnection in the terrestrial bow shock transition region. *Geophysical Research Letters*, *46*(2), 562–570. https://doi.org/10.1029/2018GL080944

Wilson, L. B., Sibeck, D. G., Breneman, A. W., Le Contel, O., Cully, C., Turner, D. L., et al. (2014). Quantified energy dissipation rates in the terrestrial bow shock: 2. Waves and dissipation. *Journal of Geophysical Research*, *119*(8), 6475–6495. https://doi.org/10.1002/2014JA019930

Wilson, L. B., Brosius, A. L., Gopalswamy, N., Nieves-Chinchilla, T., Szabo, A., Hurley, K., et al. (2021). A quarter century of wind spacecraft discoveries. *Review of Geophysics*, *59*(2), e2020RG000714. https://doi.org/10.1029/2020rg000714

Wilson, L. B., III, Chen, L.-J., Wang, S., Schwartz, S. J., Turner, D. L., Stevens, M. L., et al. (2020). Electron energy partition across interplanetary shocks. III. Analysis. Astrophys. *The Journal*, *893*(1), 22. https://doi.org/10.3847/1538-4357/ab7d39

Wilson, L. B., III, Chen, L.-J., Wang, S., Schwartz, S. J., Turner, D. L., Stevens, M. L., et al. (2019a). Electron energy partition across interplanetary shocks. II. Statistics. Astrophys. *J. Supp.*, *245*(2), 24. https://doi.org/10.3847/1538-4365/ab5445

Wilson, L. B., III, Chen, L.-J., Wang, S., Schwartz, S. J., Turner, D. L., Stevens, M. L., et al. (2019b). Electron energy partition across interplanetary shocks. I. Methodology and data product. *Astrophys. J. Supp.*, *243*(1), 8. https://doi.org/10.3847/1538-4365/ab22bd

Woods, L. C. (1969). On the structure of collisionless magneto—plasma shock waves at super—critical Alfvén—Mach numbers. *Journal of Plasma Physics*, *3*(3), 435–447. https://doi.org/10.1017/S0022377800004517

Young, D. T., Burch, J. L., Gomez, R. G., De Los Santos, A., Miller, G. P., Wilson, P., et al. (2016). Hot plasma composition analyzer for the magnetospheric Multiscale Mission. *Space Science Reviews*, *199*(1–4), 407–470. https://doi.org/10.1007/s11214-014-0119-6

Zank, G. P., Nakanotani, M., Zhao, L., Du, S., Adhikari, L., Che, H., & le Roux, J. (2021). Flux ropes, turbulence, and collisionless perpendicular shock waves: High plasma beta case. *Astrophysical Journal*, *913*(2), 127. https://doi.org/10.3847/1538-4357/abf7c8

Zhou, X., Gedalin, M., Russell, C. T., Angelopoulos, V., & Drozdov, A. Y. (2020). Energetic ion reflections at interplanetary shocks: First observations from ARTEMIS. *Journal of Geophysical Research (Space Physics)*, *125*(11), e28174. https://doi.org/10.1029/2020JA028174